Mon. Not. R. Astron. Soc. **289**, 671–680 (1997)

Neutral hydrogen at high redshifts as a probe of structure formation – III. Radio maps from *N*-body simulations

J. S. Bagla,*† Biman Nath† and T. Padmanabhan†

Inter-University Centre for Astronomy and Astrophysics, Post Bag 4, Ganeshkhind, Pune 411 007, India

Accepted 1997 April 4. Received 1997 February 24; in original form 1996 November 18

ABSTRACT

Large inhomogeneities in neutral hydrogen in the Universe can be detected at redshifts $z \leq 10$ using the redshifted 21-cm line emission. We use cosmological *N*-body simulations for dark matter and a simple model for baryonic collapse to estimate the signal expected from structures like protoclusters of galaxies at high redshifts. We study (i) the standard cold dark matter (CDM) model, (ii) a modified CDM model with less power at small scales, and (iii) a Λ + CDM model in a universe with $\Omega_0 + \Omega_\Lambda = 1$. We show that it should be possible for the next generation of radio telescopes to detect such structures at a redshift of 3.34 with an integration of about 100 h. We also discuss possible schemes for enhancing signal-to-noise ratio to detect protocondensates at high redshifts.

Key words: galaxies: formation – cosmology: theory – early Universe – large-scale structure of Universe.

1 INTRODUCTION

It is generally believed that large-scale structures, like galaxies and clusters of galaxies, formed from small initial inhomogeneities via gravitational collapse. One implication of this picture is a distinct epoch when structures like protogalaxies and protoclusters decoupled from the largely homogeneous universe. Present observations suggest that this epoch is around $z \sim 5$ for galaxies. Observations of structures in this stage of formation, if made, can be a very powerful constraint on the models of structure formation. Such observations will also improve our understanding of the process of structure formation.

Sunyaev & Zel'dovich (1972) (also see Sunyaev & Zel'dovich 1975) pointed out that the formation of first structures may be probed by observing the redshifted 21-cm line emitted by the neutral hydrogen in these structures. Several searches have been made to look for such structures at high redshifts. In the absence of a detection, these searches have only been able to put limits on the mass of neutral hydrogen present in clumped form. For a summary of these surveys see Wieringa, de Bruyn & Katgert (1992) and references cited in that paper.

*Present address: Institute of Astronomy, Madingley Road, Cambridge CB3 0HA.
†E-mail: jasjeet@ast.cam.ac.uk (JSB);
biman@iucaa.ernet.in (BN); paddy@iucaa.ernet.in (TP)

The Giant Meter-wave Radio Telescope (GMRT) presently being constructed in India should be able to improve the observational situation considerably as regards the detection and study of protocondensates containing neutral hydrogen (Swarup 1984). The GMRT will be able to probe the redshifted 21-cm line from three epochs centred at $z = 3.34$, 5.1 and 8.5. In this paper we will discuss the possibility of detection at the two lower redshifts.

Subramanian & Padmanabhan (1993) have computed the expected flux at these redshifts for some models of structure formation. They used the Press–Schechter formalism (Press & Schechter 1975) to compute the expected number densities of protoclusters in the cold dark matter (CDM) and hot dark matter (HDM) models. In a later paper (Kumar, Padmanabhan & Subramanian 1995) the authors computed line profiles assuming the protoclusters to be spherically symmetric. These studies suggest that it should be possible to detect protoclusters in the standard CDM model using the GMRT with 10 to 20 h of observations.

In this paper we use *N*-body simulations to follow the non-linear gravitational collapse of dark matter. We use some simple approximations to estimate the neutral fraction of gas in regions that have undergone collapse. We then combine these to construct 'radio maps' with same specifications as the GMRT. We will then study these maps and suggest simple methods with which to optimize the signal-to-noise ratio.

Some authors have studied the distribution of neutral hydrogen at high redshifts using simulations that include gas

dynamics, ionization and other astrophysical processes. Most of these studies focus on small-scale variations in the distribution of neutral hydrogen (see, e.g., Weinberg et al. 1996). However, the synthesized beam for the central square of the GMRT includes a large comoving volume in each pixel [approximately $8(h^{-1}\,\mathrm{Mpc})^3$] and so the details of physical processes operating at small scales can be ignored to a large extent. We can also ignore the differences in the distribution of baryons and dark matter at small scales. Further, as we are interested in the neutral fraction at two epochs, we can choose to ignore the physical processes responsible for its evolution. This simplifies the problem to a large extent and we should be able to get meaningful estimates of the signal strength without a detailed treatment of baryons and astrophyhsical processes.

A brief discussion of the expected physical conditions at the epochs of interest is given below. These are the guiding considerations in choosing the simplifying assumptions for constructing the radio maps.

(i) $z=3.34$. Observations show that the intergalactic medium (IGM) is completely ionized (Giallongo et al. 1994) at this redshift. Numerical simulations suggest that nearly all of the neutral hydrogen is in high-density, radiatively cooled objects (Weinberg et al. 1996). Observations show that a large fraction of mass in the damped lyman-α absorption systems (DLAS), believed to be progenitors of present-day galaxies, is in the form of neutral hydrogen (Wolfe et al. 1995). Observations also show that the spin temperature of gas in DLAS, the relevant quantity for the 21-cm transition, is much higher than the temperature of the background radiation at this epoch. It can be shown that, in such conditions, emission is the dominant mechanism and *the total energy emitted by radiators in such a state does not depend on the spin temperature* (Scott & Rees 1990).

(ii) $z=5.1$. We have very little information about the universe at this redshift. It is known that the intergalactic medium at redshifts $z<5$ is fully ionized (Giallongo et al. 1994). It is believed that the process of ionization is initiated by the first luminous structures in the universe. First structures like galaxies and quasars can form after $z\simeq 5$–6 in most models that satisfy other observational bounds. There are three possible scenarios that deserve mention.

(a) One possibility is that the universe is already re-ionized by $z=5.1$. In this case the neutral hydrogen will be confined to dense regions like protogalaxies and the intervening regions will be completely, or mostly, ionized.

(b) If the universe has been reheated by first luminous objects, but not re-ionized, then the spin temperature will be much higher than the temperature of the background radiation. A patchy reheating could lead to fluctuations in the 21-cm emission at large scales (Madau, Meiksin & Rees 1997).

(c) If the universe is neither reheated nor re-ionized by $z=5.1$ and the first luminous objects form around this epoch, then the spin temperature will be comparable to the temperature of the background radiation for models with $\Omega_b \leq 0.1$ (Scott & Rees 1990).

We will focus on the second scenario (for $z=5.1$) and carry out all our calculations assuming that the universe is largely neutral and the spin temperature is much larger than the temperature of the radiation background. Fluctuations in spin temperature at large scales (Madau et al. 1997) introduce uncertainty in the results as the region of interest may not have been reheated and hence the 21-cm radiation will be much less than anticipated.

2 GENERATING RADIO MAPS

We will now outline the method that is used to construct radio maps by combining the distribution of dark matter obtained from N-body simulations with approximations for the neutral fraction of gas. Radio observations with an interferometer give the flux of radiation coming from a given direction in the sky in a range of frequencies. This range of frequencies is subdivided into small equal intervals (channels). Within the field of view (primary beam) we can differentiate between flux from directions separated by an angle equal to the resolution of the interferometer (synthesized beam). Therefore we can arrange the information obtained from such an observation in terms of a radio map for each frequency channel. The angular resolution, or the pixel size, with which the map is constructed is given by the synthesized beam of the interferometer. For the purpose of generating 'radio maps' from simulations, we will choose the parameters like pixel size and channel width to be same as that used by the GMRT central array (Swarup 1984). (The central array consists of 12 antennas of diameter 45 m spread over a region of 1 km^2. The telescopes are scattered randomly within this region.)

Earlier estimates of expected flux from high redshift objects have shown protoclusters to be the most promising source (Subramanian & Padmanabhan 1993) of 21-cm radiation. Observations of high-redshift objects like quasars suggest that the intergalactic medium is completely ionized at redshifts $z<4$. This implies that the only source of neutral hydrogen will be dense clouds inside galaxies. These clouds are sufficiently dense that absorption of ionizing radiation in a thin layer near the surface shields the inner regions, and a large fraction of the gas in these remains unionized. Therefore, while computing the flux, we must take into account the fact that the neutral hydrogen we observe resides in dense clumps and shares the internal velocity dispersion of these clumps. We take this fact into account by convolving the line profile with a Gaussian of width 200 km s^{-1}, at the epoch of emission. This consideration is relevant only for the window at $z=3.34$, as in most models galaxies have not formed by $z=5.1$. Any protogalaxies that may exist are not expected to have any systematic velocity dispersion.

A remaining uncertainty in computing the amount of neutral hydrogen at high redshifts is the fraction of mass in galaxies at the epoch of interest. We will *reduce* the uncertainty due to this factor by considering only the regions with $\delta>1$ in the numerical simulations. (Changing this threshold to $\delta>3$ reduces the peak signal by less than 15 per cent, therefore the final result is not very sensitive to this threshold.) However, since this is a complex issue, we will only parametrize our ignorance with a factor f_{gal}, which is the fraction of mass in galaxies that can hold neutral hydrogen. We will use $f_{\mathrm{gal}}=1$, but the results can be re-scaled with any value. In a more detailed calculation, which can be done

with N-body simulations that use a much larger number of particles, individual haloes of mass $M \geq 10^{10}\,M_\odot$ can be directly identified and the uncertainty parametrized by f_{gal} becomes irrelavant. This cannot be done at present without reducing the physical size of the simulation box by a significant amount – in which case we will not be able to map all scales probed by the GMRT.

The radio map is generated from the N-body data in the following manner.

(i) Use the coordinates of the particle to fix the pixel to which the contribution is to be added.

(ii) Use the radial component peculiar velocity of the particle to compute the total redshift. Convolve the line profile with a Gaussian of width 200 km s^{-1} and add the contribution to the relevant frequency channels.

(iii) For generating maps at redshifts $z < 4$, impose a cut-off on density contrast $\delta \geq 1$ to ensure that we are looking at regions that can host galaxies.

(iv) Repeat this process for all particles.

In the following subsections we will describe each of these components in greater detail. We begin by outlining the models of structure formation that are used for this study.

2.1 *N*-body simulations

We use N-body simulations of three models to generate the 'radio maps'. These were chosen from the family of CDM models and we used the parametrized spectrum given by Efstathiou, Bond & White (1992). These models were normalized using the root mean square amplitude of fluctuations in the temperature of the cosmic microwave background radiation (CMBR) observed by *COBE* (Wright et al. 1996).

All the simulations were carried out using 128^3 particles in a 128^3 mesh. The physical size of the box in each case was $128\,h^{-1}$ Mpc. Thus the mass of each particle in these simulations equals $2.7 \times 10^{11}\,\Omega_0\,M_\odot$.

The following parameters were chosen for these models.

(i) Model I: the standard CDM model (sCDM). ($\Gamma = \Omega_{nr} h = 0.5$, where the density parameter for non-relativistic matter $\Omega_{nr} = \Omega_0 = 1$ and $h = 0.5$.) Normalization with fluctuations in the CMBR gives $\sigma(8\,h^{-1}\,\mathrm{Mpc}, z = 0) \simeq 1.2$, which is about twice the value implied by the abundance of rich clusters. This model is a reference model in studies of structure formation.

(ii) Model II: a flatter version of the CDM model with $\Gamma = 0.3$, $\Omega_{nr} = \Omega_0 = 1$ and $h = 0.5$. The choice of Γ for this model is independent of the cosmological parameters. This model has $\sigma(8\,h^{-1}\,\mathrm{Mpc}, z = 0) \simeq 0.6$, which is consistent with the observed amplitude of fluctuations at this scale. This model also predicts the correct slope of the correlation function at large scales. At large scales this model is a close approximation for some 'flat' versions of CDM that can arise if a small but non-negligible fraction of mass in the universe is contributed by relativistic dark matter (mixed dark matter or MDM hereafter).

(iii) Model III: a Λ+CDM model (LCDM). ($\Gamma = \Omega_{nr} h = 0.3$, $\Omega_{nr} = 0.6$, $\Omega_\Lambda = 0.4$ and $h = 0.5$.) This model has $\sigma(8\,h^{-1}\,\mathrm{Mpc}, z = 0) \simeq 1$, which is also consistent with the observed abundance of rich clusters. [The observed amplitude of fluctuations at the scale of $8\,h^{-1}$ Mpc scale approximately at $\Omega_{nr}^{-0.6}$ (White, Efstathiou & Frenk 1992).] This model satisfies most observational constraints that are available for cosmological models and models of structure formation (Bagla, Padmanabhan & Narlikar 1996). (These constraints rule out large regions of the parameter space and only a small region survives, therefore model III is a good example from the class of allowed models.) This model was chosen for two reasons.

(1) The growth of perturbations in a Λ model slows down at late epochs. In other words, such a model has more power at early times in comparison with an $\Omega_{nr} = 1$ universe which has the same level of clustering at $z = 0$. Thus we have reason to expect a higher signal for models in a universe with non-zero Λ.

(2) The comoving volume enclosed in a given solid angle at high redshifts is higher for a universe with non-zero Λ. This implies more emitters and hence a higher signal. In a model with a non-zero cosmological constant, the luminosity distance is also larger in comparison with the corresponding distance in the Einstein–de Sitter model for any given redshift. However, the increase in comoving volume mentioned above compensates for the increase in luminosity distance in such models.

We have shown the power spectra for these models in Fig. 1. To demonstrate the effect of a different rate of growth in a linear regime we have also shown the same spectra at redshift 3.34.

We would like to emphasize the following points regarding the choice of models: it is possible to choose many variants of the above models and repeat the analysis given in this paper. One can choose to normalize the power spectra in a different manner, e.g. by fixing the amplitude of perturbations at $8\,h^{-1}$ Mpc rather than at very large scales using *COBE* observations. Other parameters like the Hubble constant, the cosmological constant, the density parameter and the primordial spectral index can also be varied from the values used here. We have consciously restricted ourselves to a small set of example models for the purpose of illustation. A more detailed exercise will be warranted if the GMRT succeeds in detecting neutral hydrogen at these redshifts and a more meaningful comparison with models can be carried out using real data.

2.2 Evolution of the neutral fraction

Generating artificial radio maps requires, in principle, a detailed knowledge of the distribution of baryons and the neutral fraction, etc. However, as mentioned earlier in this paper, the comoving volume enclosed in each pixel is very large and therefore we can get reasonable estimates by assuming the distribution of baryons and dark matter to be the same. In the following discussion we will demonstrate, using a simple model, that the assumption of a constant neutral fraction at these scales is not very far from the truth. We will also show that our choice of $f_N = 0.5$ for $z = 3.34$ is not unrepresentative. We will show that the neutral fraction of gas in galaxies is largely independent of the depth of the potential well. In the following discussion we estimate the neutral fraction by using the model of star formation in

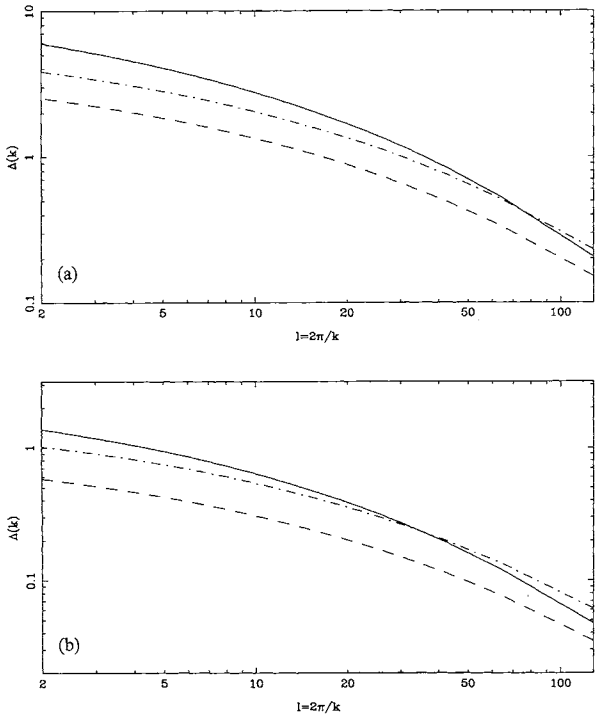

Figure 1. This figure shows the power spectra for the three models being discussed here. The standard CDM model is shown using a thick line, model II (MDM) as a dashed line and model III (LCDM) as a dot–dashed line in these panels. We have shown the linearly evolved power spectrum at the present spoch (a) and also at the redshift $z=3.34$ (b). The different rate of growth for model III (LCDM) in the linear regime leads to an increase in the ratio of power in this model to the power in model I (sCDM) or model II (MDM).

galaxies of Kauffmann, White & Guiderdoni (1993; hereafter KWG). Here we will briefly summarize the relevant features of their model and use these to estimate the evolution of the neutral fraction.

In this model, dark matter haloes are assumed to be truncated singular isothermal spheres, and it is assumed that the temperature T of the gas is given in terms of the circular velocity, V_c, as, $T=35.9\ (V_c\ \mathrm{km\ s^{-1}})^2\ \mathrm{K}$. The virial radius r_v is defined to be the radius within which the mean overdensity is 200 [i.e., $r_v=0.1\,H_0^{-1}(1+z)^{-3/2}V_c$]. The radius where the cooling time of the gas is equal to the age of the universe is defined as the cooling radius, r_{cool}.

Suppose that the fraction of the critical density that is in baryons is Ω_b, and f_g is the fraction of the baryons in the form of gas. The amount of cold gas inside the halo at time t is given by the amount of gas with cooling time $t_{cool}<t$. When $r_{cool}\gg r_v$, cooling is very rapid and the rate of increase of cold gas in the halo is governed by the accretion rate of the halo (White & Frenk 1991),

$$\dot{M}_{inf}(V_c,z)=0.15 f_g \Omega_b V_c^3 G^{-1}. \tag{1}$$

In the other limit, $r_{cool}\ll r_v$, the rate of inflow of cold gas can be written as

$$\dot{M}_{cool}(V_c,z)=4\pi\rho_g(r_{cool})r_{cool}^2\frac{dr_{cool}}{dt}, \tag{2}$$

where $\rho_g(r)$ is the gas density at radius r.

In the model of KWG, the rate at which cold gas settles inside the halo is given by $\min(\dot{M}_{inf}, \dot{M}_{cool})$. For the cooling of the gas, we use the cooling function of Fall & Rees (1985) for a primordial gas, since the metallicity is in any case small for gas at high redshift.

However, with the onset of star formation, the supernovae will begin to heat the gas. Following KWG, we assume that the number of supernovae per solar mass of star formed is $\eta_{SN}=4\times10^{-3}\,M_\odot^{-1}$. If each of the supernopvae has a kinetic energy of the ejecta of over 10^{51} erg, and a fraction ϵ of this energy is used to heat the cold gas, then the rate of loss of cold gas to the hot phase of the interstellar medium is (KWG)

$$\dot{M}_{reheat}=\epsilon\frac{4}{5}\frac{\dot{M}_*\eta_{SN}E_{SN}}{V_c^2}. \tag{3}$$

Here, $\dot{M}_*$ is the star formation rate, which is given in this model as

$$\dot{M}_*=\alpha\frac{M_{cold}}{t_{dyn}}. \tag{4}$$

Here t_{dyn} is the dynamical time. The authors defined the dynamical time as (where $\lambda\sim0.05$ is the initial dimensionless spin parameter of the gas),

$$t_{dyn}=\frac{r_{gal}}{V_{gal}}=\frac{(2\lambda r_v)^{3/2}}{(GM_{gal})^{1/2}}. \tag{5}$$

These equations govern the evolution of the amount of cold gas, or, in other words, the neutral fraction, f_{H_I}, of gas in a halo of circular velocity V_c at a given redshift z, for an assumed value of the onset of inflow of gas z_{in}, and given the values of α and ϵ. Gas is assumed to be fully ionized at z_{in}. KWG estimated the values of α and ϵ from evolving the stellar population according to the above model and comparing the mean luminosity and the cold gas content of haloes of $V_c=220\ \mathrm{km\ s^{-1}}$ with the observed values for the Milky Way (their table 1). For example, for $\Omega_0=1$, $\Omega_b=0.1$, $\alpha=0.1$ and $\epsilon=0.08$. The values of α and ϵ are smaller for smaller values of Ω_b. However, we have found that the neutral fraction is not very sensitive to the values of α and ϵ, but rather is sensitive to z_{in}.

We plot in Fig. 2 the neutral fraction f_{H_I} at $z=3.34$ for $z_{in}=4$, 5, 6, 9, as functions of the rotational velocity V_c. It is seen that the neutral fraction is not sensitive to the value of V_c, for $V_c>150\ \mathrm{km\ s^{-1}}$. We will, therefore, use a constant value of f_n for all potential wells. We also show the values of f_{H_I} at $z=5.1$ for $z_{in}=6$, 9 as function of V_c in Fig. 2. The neutral fraction f_n does not depend very strongly on the value of $f_g\Omega_b$. In the following discussion we will use $f_n=0.5$.

2.3 Redshift space projection

Simulations output the data in the form of positions and velocities of particles, whereas radio observations detect the flux as a function of angular position and frequency. In this subsection we will outline the method used for computing the observed central frequency around which the 21-cm

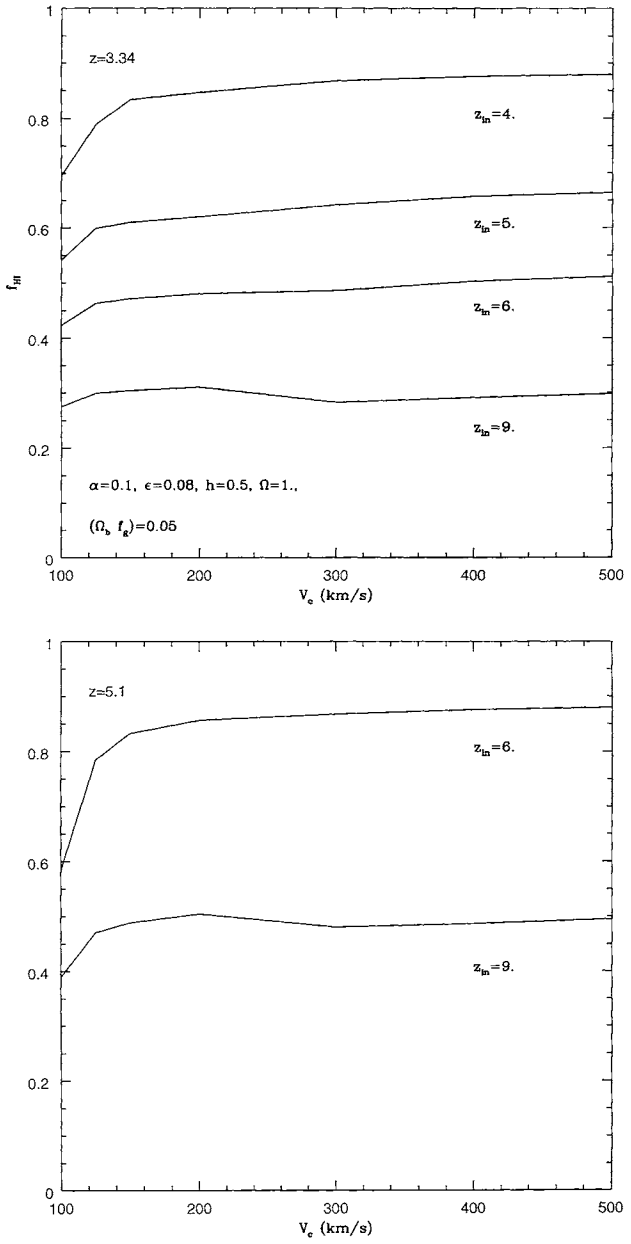

Figure 2. Panel (a) shows neutral fraction f_{H_I} at $z=3.34$ against the circular velocity V_c of the halo for $z_{in}=4, 5, 6, 9$. We have assumed $\alpha=1$, $\epsilon=0.08$, $f_g\Omega_b=0.05$, $h=0.5$ and $\Omega=1$. Here, f_g is the fraction of baryonic mass in the form of gas. The curves do not strongly depend on the value of f_g. Panel (b) similarly plots the neutral fraction at $z=5.1$ for $z_{in}=6, 9$.

radiation from hydrogen atoms represented by a given N-body particle is observed.

The peculiar velocity of an N-body particle is given by

$$v_p = a\dot{a}\frac{dx}{da} = H_0 a^2 \frac{H(a)}{H_0}\frac{dx}{da}. \tag{6}$$

We only need the radial component of velocity for computing the redshift. As we are dealing with particles at very high redshifts, we can align one axis of the simulation box along the line of sight and use that component of velocity for computing the recession velocity. The ratio of H/H_0 is given by

$$\frac{H(a)}{H_0} = \frac{\Omega_{nr}}{a^3} + \Omega_\Lambda \tag{7}$$

for the models of interest. The effective redshift results from a combination of the Hubble recession and the peculiar velocity

$$1 + z_{tot} = (1 + z_{hub})(1 + z_{pec}). \tag{8}$$

The average z_{hub} for the simulation box is $1/a - 1$. Redshift due to peculiar velocity is given by $z_{pec} = v_p/c$ where c is the speed of light.

2.4 Flux

If the spin temperature of the atoms emitting 21-cm radiation is much greater than the temperature of the CMBR, then the spin temperature drops out of the expression for the emitted energy. In such a case the energy dE emitted by a set of hydrogen atoms in an interval dt_e is given by

$$dE = \text{rate of transition} \times \text{energy carried by a photon} \times \text{number of hydrogen atoms} \times dt_e$$

$$= \frac{3}{4} A_{21} \times h\nu_e \times \frac{M_{H_I}}{m_p}\, dt_e \tag{9}$$

where m_p is the mass of a proton and M_{H_I} is the total mass in neutral hydrogen. We will use the mass in neutral hydrogen contributed by one particle in the N-body simulation to compute total energy emitted by each 'N-body particle'. The mass M_{H_I} is given by

$$M_{H_I} = M_{part} f_b f_n = M_{part} \frac{\Omega_b}{\Omega_0} f_n$$

$$= 8.1 \times 10^9\, M_\odot \left(\frac{\Omega_b}{0.06}\right)\left(\frac{f_n}{0.5}\right), \tag{10}$$

where f_b is the fraction of baryons, Ω_b is the contribution of baryons to the density parameter and f_n is the neutral fraction. We have chosen $\Omega_b=0.06$ as this value compares well with the observed abundance of light elements and primordial nucleosynthesis (Copi, Schramm & Turner 1995). Using this, we can estimate the flux received by an observer from an 'N-body particle'. For $\Omega_{nr}=\Omega_0=1$ models, the flux contributed by one particle at redshift $z=3.34$ is given by

$$S_\nu = 1.1\ \mu\text{Jy} \left(\frac{M_{H_I}}{8.1 \times 10^9\, M_\odot}\right)\left(\frac{\Delta v_{\frac{1}{2}}}{175\ \text{kHz}}\right)^{-1}. \tag{11}$$

The frequency width used here corresponds to a velocity dispersion of 200 km s^{-1}. (The corresponding number for the model with $\Omega_\Lambda=0.4$ is 0.77 μJy.

3 RESULTS

In this section we shall outline the results of the analysis of the radio maps generated from N-body simulations. We

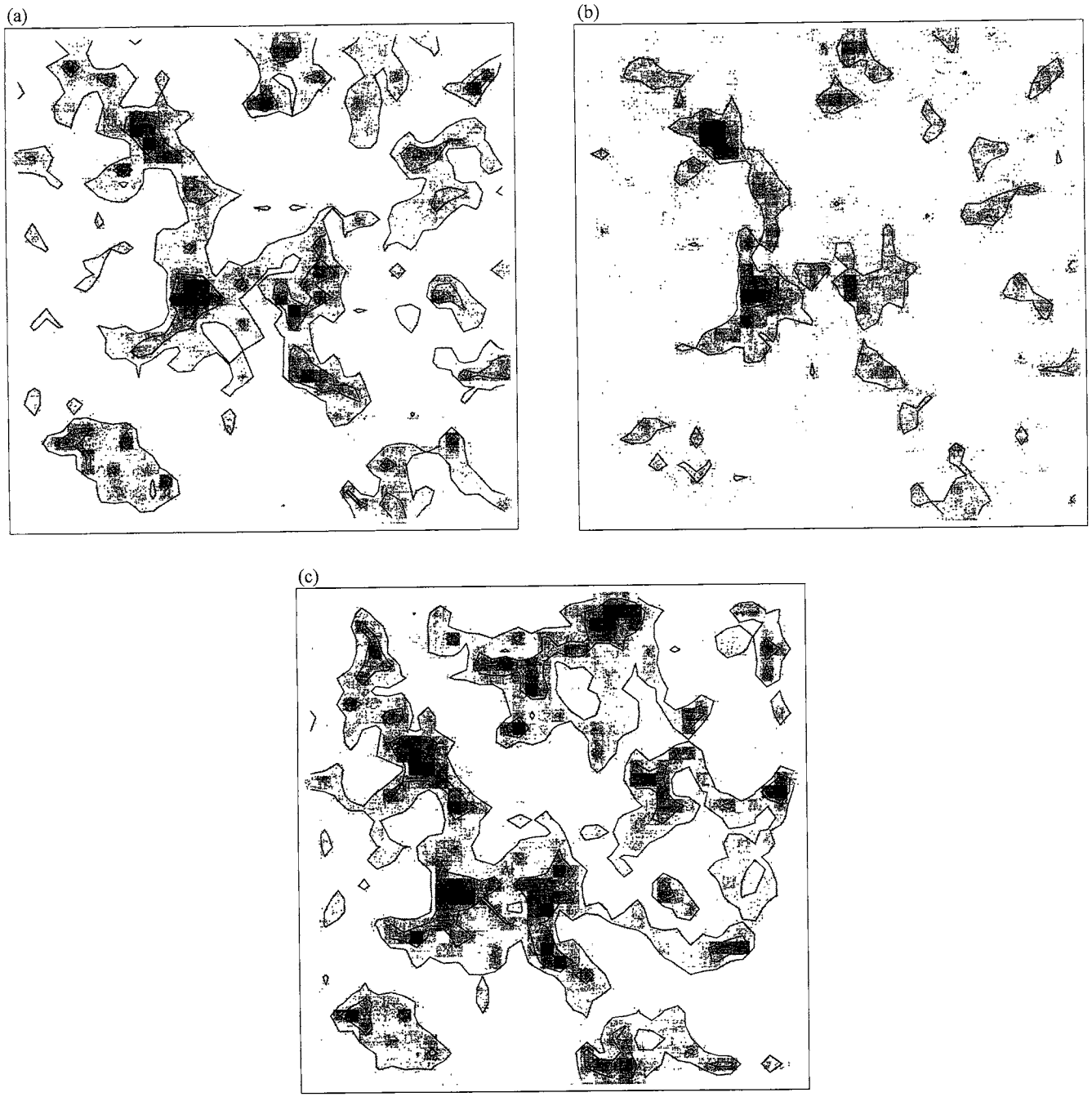

Figure 3. Panel (a) shows a sample radio map for model I (sCDM) at redshift $z=3.34$. This map is shown for one frequency channel of width 125 kHz (corresponding to a velocity width of 115 km s^{-1}). Each pixel corresponds to an angular resolution of 3.2 arcmin and a physical scale of about 3 h^{-1} Mpc. The contour levels correspond to 15, 30 and 60 μJy. (b) Sample map for model II (MDM). (c) Sample map for model III (LCDM).

begin with a pictorial preview of the radio maps. Fig. 3 shows a sample radio map for each of the three models at redshift $z=3.34$. The panels of this figure show one frequency channel (chosen to be 125 kHz, which – in velocity units – corresponds to about 115 km s^{-1}). The contours in these radio maps correspond to 15, 30 and 60 μJy. The pixel size is 3.2 arcmin and it corresponds to a comoving scale of 2.7 h^{-1} Mpc for models I and II. (3.5 h^{-1} Mpc for model III.) It is clear from these panels that models I (sCDM) and III (LCDM) have comparable signal whereas model II (MDM), as it has less power at smaller scales, has somewhat lower signal. The profile of peaks in the sCDM model is steeper than that in the LCDM model.

Fig. 4 shows similar maps for $z=5.1$ [$\nu_0=233$ MHz]. The width of one channel in this case corresponds to a velocity width of 161 km s^{-1}. Angular size of each pixel is 4.5 arcmin and this corresponds to a comoving scale of 4.7 h^{-1} Mpc for models I (sCDM) and II (MDM), and one of 5.4 h^{-1} Mpc for model III (LCDM). These maps clearly show that ther are no small-scale structures in these, in comparison with

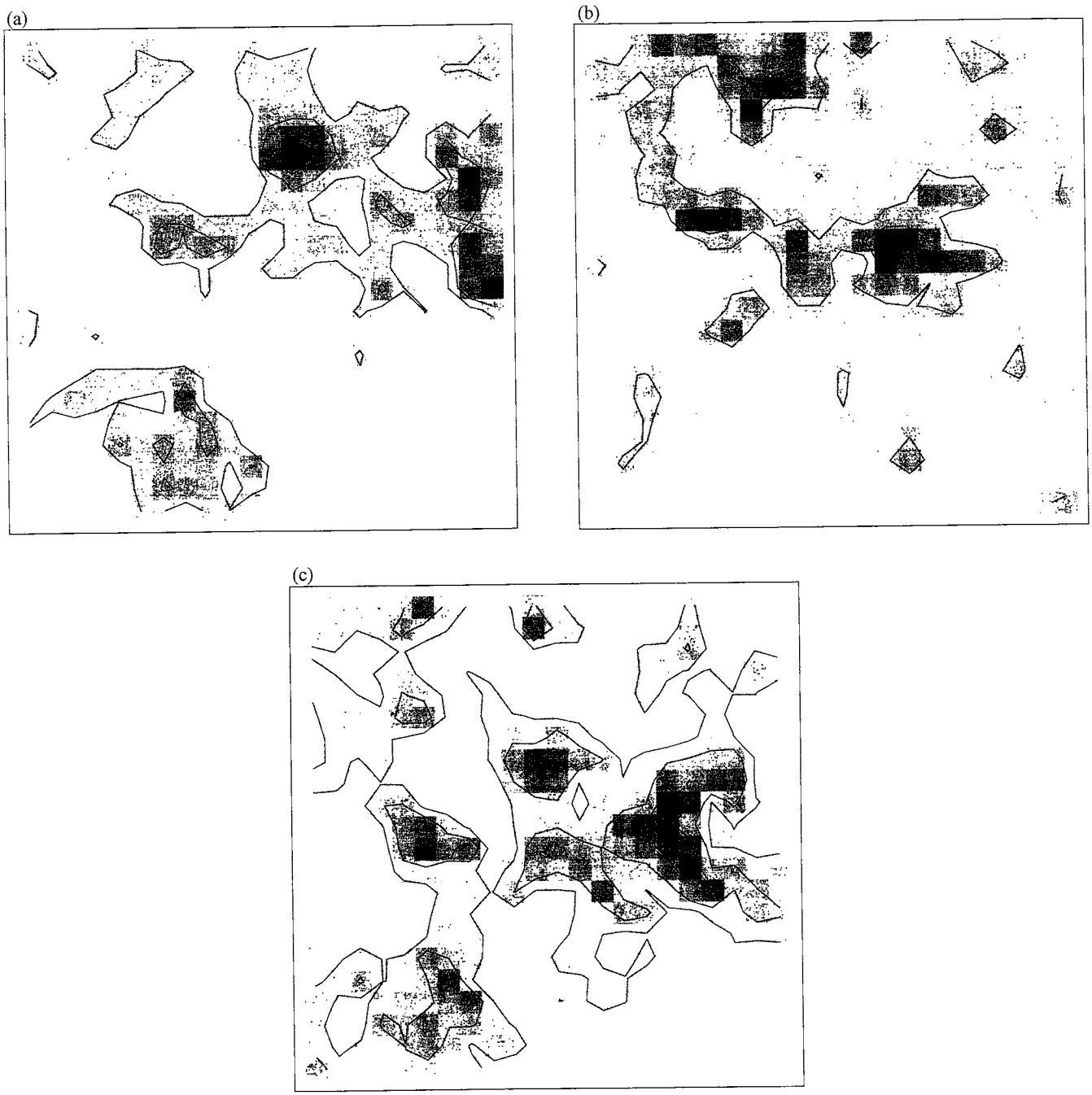

Figure 4. (a) This figure shows a sample radio map for model I (sCDM) at redshift $z=5.1$. This map is shown for one frequency channel of width 125 kHz (corresponding to a velocity width of 160 km s^{-1}). Each pixel corresponds to an angular resolution of 4.5 arcmin and a physical scale of about 5 h^{-1} Mpc. The contour levels correspond to 40, 80, 120 and 200 μJy. (b) Sample map for model II (MDM). (c) Sample map for model III (LCDM).

the maps at $z=3.34$. One reason for the gentler variation in signal from one pixel to another arises from the fact that, having assumed that the IGM is not ionized, we have not discarded matter in underdense regions while computing the signal. The signal is much higher as the comoving volume enclosed in each pixel/channel is larger than the corresponding volume at redshift 3.34.

These qualitative features can also be seen in Fig. 5, which shows a sample spectrum from the simulations of model III (LCDM) at these two redshifts. The spectra are shown as a function of channel number and the signal is shown in μJy. The typical width of high peaks seen in these graphs is much larger than the velocity dispersion of 200 km s^{-1} ascribed to individual particles.

In order to make quantitative estimates of the possibility of detecting neutral hydrogen at high redshifts, we computed the amplitude of the three highest peaks in the radio maps for the three models. Table 1 lists the amplitudes and

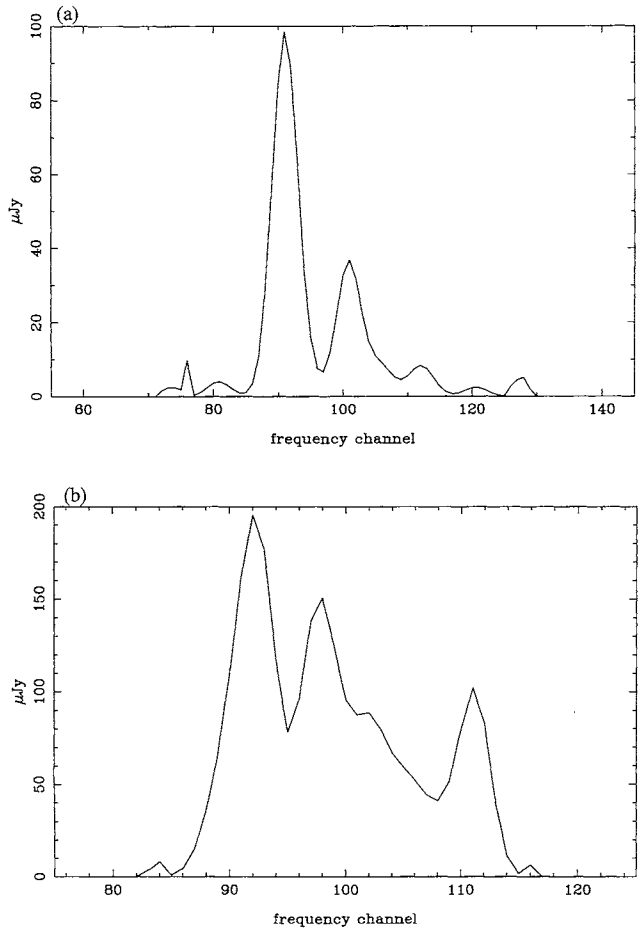

Figure 5. This figure shows a sample spectrum for each of the redshifts. The spectra shown here are taken from the simulated radio maps of the LCDM model (model III). Panel (a) corresponds to $z=3.34$ and the panel (b) to $z=5.1$. This signal in μJy is shown as a function of frequency channel [channel width = 125 kHz]. This figure shows that the signal at $z=5.1$ has few small-scale variations in comparison with the signal at $z=3.34$.

Table 1. This table lists details of three highest peaks in the simulated radio maps for the three models of structure formation being considered here for the redshift window at $z=3.34$ (327 MHz). We have listed the amplitude of peaks in microJanskys, full width at half maximum in MHz and the number of pixels enclosed in the contours of half maximum. It is clear that models I (sCDM) and III (LCDM) have a higher signal as compared to model II (MDM).

Model	Amplitude (μJy)	FWHM (MHz)	n_{HM}
I	137.2	1.5	3
	101.5	1.0	11
	99.8	0.875	7
II	87.1	1.0	6
	97.7	0.75	8
	93.5	0.875	12
III	124.6	0.875	11
	111.3	0.875	13
	103.8	1.125	8

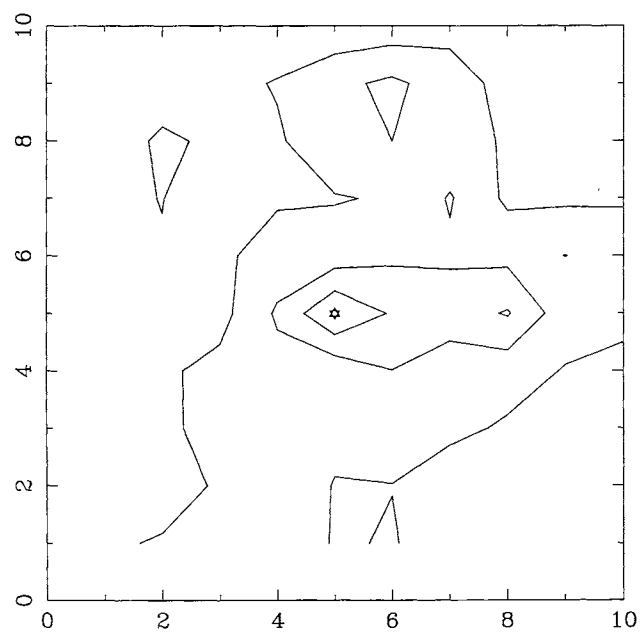

Figure 6. This figure shows the contours for $f*S_{max}$ around a peak for $f=0.75$, 0.5 and 0.25. These contours are for one of the highest peaks in simulated maps for model III (LCDM). The peak is located at (5, 5) in this picture and is marked by a star. It is clear from this figure that the signal can be averaged over neighbouring pixels to improve signal-to-noise ratio. However, the shape of this

the full width at half maximum (FWHM) for these models for the three highest peaks in each case at redshift 3.34. The last column lists the number of pixels enclosed within the contours of half maximum. The contours were drawn for signal averaged over frequency channels. The number of channels used for averaging was taken to be the FWHM for the relevant peak. This number (n_{HM}) indicates the typical angular size of a flux peak, and the signal can be smoothed at this scale to enhance the signal-to-noise ratio. However, the shapes of these peaks are somewhat arbitrary and it is difficult to suggest a generic smoothing function for improving the chances of detection. Fig. 6 shows contours around one such peak, showing the level at which the signal drops to 0.75, 0.5 and 0.25 of its maximum value. This figure demonstrates the point mentioned above regarding the shapes of these contours.

Even though we cannot suggest the most optimum smoothing function for improving the signal-to-noise ratio, we have confirmed that the signal-to-noise ratio does improve for smoothing with a square top-hat window of size $\approx n_{HM}^{1/2}$ where n_{HM} is the number of pixels enclosed within the contour of $S_{max}/2$. We assumed that the noise scales as $n^{-1/2}$ for small n. The signal-to-noise ratio for models II (MDM) and III (LCDM) can be improved by a factor of two in this manner. The standard CDM model [model I] has more small-scale power and hence the peaks are much sharper, and therefore the gain in signal-to-noise ratio by smoothing is somewhat limited in this case.

In order to estimate the integration time required for detection and imaging of these peaks we need to know the root mean square amplitude of noise expected for the

GMRT receivers. The expected noise for the central array is

$$\text{rms noise} = 44\ \mu\text{Jy}\left(\frac{T_s}{100\ \text{K}}\right)\left(\frac{1\ \text{MHz}}{\Delta\nu}\right)^{1/2}\left(\frac{100\ \text{h}}{\tau}\right)^{1/2}$$

$$= 100\ \mu\text{Jy}\left(\frac{T_s}{250\ \text{K}}\right)\left(\frac{1\ \text{MHz}}{\Delta\nu}\right)^{1/2}\left(\frac{100\ \text{h}}{\tau}\right)^{1/2}. \qquad (12)$$

The system temperaturte for the 327 MHz window is 110 K and the corresponding number for 233 MHz is 250 K (Swarup 1984).

It is clear from Table 1 that the peak signal expected in models I (sCDM) and III (LCDM) is about three times larger than the rms noise expected at redshift 3.34. Further, the width of the peaks in frequency space is comparable to 1 MHz. The signal-to-noise level can be enhanced further by smoothing over nearby pixels. The number of pixels enclosed in the contour of $S_{max}/2$ for model III (LCDM) varies between 8 and 13 for the three higher peaks listed in Table 1. Therefore, an enhancement by a factor of two or more can be obtained by smoothing over nearby pixels. This implies that a 3σ detection of such objects should be possible with an integration time of 50–100 h. The main uncertainty in this result comes from our lack of knowledge about the fraction of mass in galaxies. We have, of course, tried to reduce the uncertainty by using only regions with a density contrast greater than unity for computing the signal. As mentioned before, we find that changing the density threshold to $\delta_c = 3$ does not change the amplitude of the highest peaks by more than 15 per cent. However, as the estimated signal and noise have a similar amplitude, even a small factor may make all the difference.

The detection of neutral hydrogen at high redshift for model I (sCDM) should also require a similar integration time. Here the frequency spread of the highest peak is very large and compensates, to some extent, for the compactness of the peak in angular coordinates. On the other hand, the detection of neutral hydrogen in model II (MDM) is a more difficult proposition as the peak signal is small compared to that for the other two models. The integration time required for model II (MDM) is at least twice as large as that for models I (sCDM) and III (LCDM).

Table 2 lists the amplitude of the three highest peaks for the three models we are using here for the window at redshift 5.1. We have also listed the full width at half maximum for each of these peaks. These peaks have a very shallow profile and the number of pixels, enclosed within the region where the signal is greater than half of the maximum value, can be very large. Therefore we can smooth the signal over a few neighbouring pixels and improve the signal-to-noise ratio by a significant amount. Results for different models in this case are:

(i) model III (LCDM) predicts a signal that is comparable to the rms noise. Smoothing over nearby pixels and integration for 50–100 h should be sufficient for a 3σ detection;

(ii) model I (sCDM) also predicts signal at the same level as model III (LCDM);

(iii) model II (MDM) has a very low signal as compared to models I (sCDM) and III (LCDM) and will require an integration for 100–200 h for a 3σ detection.

Table 2. This table lists details of three highest peaks in the simulated radio maps for the three models of structure formation being considered here for the redshift window at $z = 5.1$ (233 MHz). We have listed the amplitude of peaks in micro-Janskys and full width at half maximum in MHz. It is clear that models I (sCDM) and III (LCDM) have a higher signal as compared to model II (MDM).

Model	Amplitude (μJy)	FWHM (MHz)
I	199.0	0.75
	181.4	1.0
	163.2	0.625
II	138.6	0.75
	115.2	0.875
	103.8	0.75
III	221.7	0.75
	195.6	0.875
	153.9	0.875

These numbers, however, must be considered in the light of the possibility of patchiness in reheating of the IGM (Madau et al. 1997).

4 DISCUSSION

The results of numerical simulations suggest that it could be possible to detect neutral hydrogen at high redshifts in protoclusters. The detection of these objects with the GMRT will require integration over 50–100 h. The signal-to-noise ratio for $z = 3.34$ is better than that expected for $z = 5.1$ if we choose the factor f_{gal} to be unity. This is the most uncertain number in our calculation. If this number is much smaller than unity then it may be difficult to image protoclusters at this redshift. It may be possible to 'detect' neutral hydrogen statistically by doing a $(\Delta T)/T$ type of experiment. In these, one looks for excess correlations beyond those that would be expected from noise in the instrument. For example, the emission from a region of size $10^6 (h^{-1}\ \text{Mpc})^3$ – the typical size of the volume probed in one field of view – is around 370 mJy. (This number is obtained by using the average flux in the simulated radio maps.) This will appear as excess noise if the individual structures can not be imaged. Integration over more than one field of view can also be used to enhace the chances of detection, as one may be able to pick up a rare density peak (Subramanian & Padmanabhan 1993).

As mentioned above, the largest uncertainty in our results for $z = 3.34$ is introduced by our lack of knowledge about f_{gal}. This uncertainty can only be removed with large simulations that can resolve masses less than $10^{10}\ M_\odot$ and still cover a volume that is comparable to that covered by one field of view for the GMRT. The other option is to carry out a series of N-body experiments at different scales for each of the models and deduce f_{gal} for each model from the ensemble of simulations.

A comparison with earlier estimates for the expected signal (Kumar et al. 1995) shows that the highest signal

obtained in simulations is smaller than that expected from a protocluster of mass $10^{15}\,M_{\odot}$. This could be the result of three factors:

(i) we do not have a sufficienlty high peak in our realization of the density field;
(ii) the angular extent of the protoclusters is considerably larger than one pixel; and
(iii) the velocity dispersion of these clusters is larger than expected.

We feel that all of these factors have contributed to make our estimates smaller than the earlier estimates by a factor of 2–5.

The possibility of the detection of neutral hydrogen at redshift 5.1 may be easier if the universe has been reheated but not fully re-ionized. Another good feature of 21-cm emission from this epoch is that it only has smooth large-scale variations in signal and hence it should be possible to enhance the signal-to-noise ratio by at least a factor of 2–3 by smoothing over nearby pixels. However, the results for this epoch are somewhat uncertain due to our poor knowledge of the physical conditions at $z > 5$.

ACKNOWLEDGMENTS

The authors thank K. Subramanian and J. Chenglur for useful discussions. JSB thanks CSIR India for financial support.

REFERENCES

Bagla J. S., Padmanabhan T., Natlikar J. V., 1996, Comments on Astrophysics, 18, 275
Copi C. J., Schramm D. N., Turner M. S., 1995, Sci., 267, 192
Fall S. M., Rees M. J., 1985, ApJ, 298, 18
Efstathiou G., Bond J. R., White S. D. M., 1992, ŃRAS, 258, 1P
Giallongo E., D'Odorico S., Fontana A., McMahon R. G., Savaglio S., Cristiani S., Molaro P., Trevese D., 1994, ApJ, 425, L1
Kauffman G., White S. D. M., Guideroni B., 1993, MNRAS, 264, 201 (KWG)
Kumar A., Padmanabhan T., Subramanian K., 1995, MNRAS, 272, 544
Madau P., Meiksin A., Rees M. J., 1997, ApJ, 475, 429
Press W. H., Schechter P., 1975, ApJ, 475, 429
Press W. H., Schechter P., 1975, ApJ, 187, 452
Scott D., Rees M. J., 1990, MNRAS, 247, 510
Subramanian K., Padmanabhan T., 1993, MNRAS, 265, 101
Sunyaev R. A., Zeldovich Ya. B., 1972, A&A, 20, 189
Sunyaev R. A., Zeldovich Ya. B., 1975, MNRAS, 171, 375
Swarup G., 1984, Giant Meter-Wavelength Radio Telescope – Proposal. Radio Astronomy Centre, TIFR, India
Weinberg D. H., Hernquist L., Katz N. S., Miralda-Escudé J., 1996, in Bremer M., Röttgering H., Carilli C., van de Werf P., eds, Cold Gas at High Redshift. Kluwer, Dordrecht
White S. D. M., Efstathiou G., Frank C. S., 1992, MNRAS, 262, 1023
White S. D. M., Frenk C. S., 1991, ApJ, 379, 52
Wieringa M. H., de Bruyn A. G., Matgert P., 1992, A&A, 256, 331
Wolfe A. M., Lanzetta K. M., Foltz C. B., Chaffee F. H., 1995, ApJ, 454, 698
Wright E. L., Bennet C. L., Gorski K., Hinshaw G., Smoot G. F., 1996, ApJ, 464, L21